J. Fluid Mech. (2023), *vol*. 959, A41, doi:10.1017/jfm.2023.180

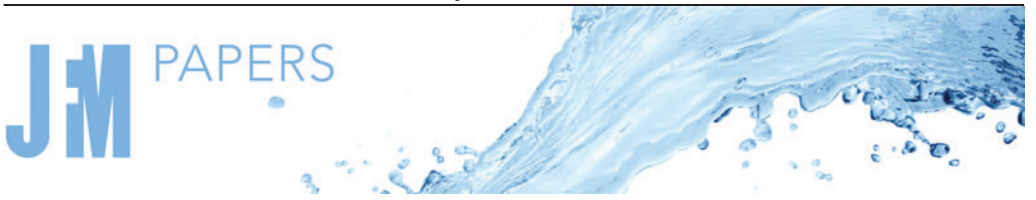

Collapse of a cohesive granular column

A. Gans[1], A. Abramian[2], P.-Y. Lagrée[2], M. Gong[3], A. Sauret[3], O. Pouliquen[1] and M. Nicolas[1],†

[1]CNRS, IUSTI, Aix Marseille Université, Marseille, France

[2]CNRS, Institut Jean le Rond d'Alembert, Sorbonne Université, Paris, France

[3]Department of Mechanical Engineering, University of California, Santa Barbara, CA 93106-5070, USA

(Received 5 July 2022; revised 14 February 2023; accepted 18 February 2023)

The collapse of a quasi-two-dimensional column of cohesive granular media is investigated experimentally and numerically in the framework of a continuum model. The configuration is an initial parallelepiped-shaped granular pile, which is suddenly released by opening a retaining door. The experiments rely on a model material developed by Gans *et al.* (*Phys. Rev.* E, vol. 101, 2020, 032904) made of silica particles coated with polyborosiloxane, for which the adhesive interparticle force can be tuned by controlling the thickness of the coating. Numerically, the collapse is simulated using a simple cohesive rheological model implemented in a two-dimensional Navier–Stokes solver. We investigate the role of cohesion on the stability of the column, the mode of failure, the flow dynamics and the geometry of the final deposit. Our results show that the continuum model captures the main features observed experimentally.

Key words: wet granular material, rheology

1. Introduction

Cohesive granular materials are encountered in many geophysical and industrial applications. Whereas many advances have been made in the description of cohesionless granular flows in various configurations, the behaviour of cohesive granular media has been much less investigated. One difficulty is the complexity underlying the origin of cohesion. For very small particles (typically below 10 μm in diameter), the cohesion arises from attractive forces like van der Waals (Castellanos 2005) or electrostatic forces (Konopka & Kosek 2017), whereas for larger particles it may arise from capillary bridges (Bocquet *et al.* 1998; Mitarai & Nori 2006) or from solid bridges (Langlois, Quiquerez & Allemand 2015). In some situations, adhesive force between grains may also evolve due to variations in the environmental conditions (change of the confinement pressure, the

† Email address for correspondence: maxime.nicolas@univ-amu.fr

temperature or the humidity rate) or due to the micromechanical evolution of the bonds (ageing, sintering, chemical reaction) (Kamiya *et al.* 2002; Foster, Bronlund & Paterson 2006).

This complexity in controlling cohesion explains why most of the fundamental experimental studies focus on wet granular materials, for which cohesion is controlled by the amount of liquid mixed with the grains. Different canonical configurations, such as flow in rotating drums or granular collapse, have been investigated using unsaturated wet granular media. However, capillary bridges are known to migrate and merge during flow, which adds some heterogeneities and complexity to the flow. Recently, a new model granular material has been developed, where the cohesion originates from a polyborosilicate (PBS) coating of glass particles (Gans, Pouliquen & Nicolas 2020). The resulting cohesive material is very stable and reusable; the adhesive force is constant in time and is simply controlled by the thickness of the coating. This material has been used, for instance, to study the erosion of a cohesive granular bed by a turbulent jet by (Sharma *et al.* 2022). In this study, we investigate the dynamics of this cohesion-controlled granular material (CCGM) in the classical configuration of granular collapse.

Granular collapse, which consists of the sudden release of a granular pile under gravity (Balmforth & Kerswell 2005; Lajeunesse, Monnier & Homsy 2005; Lube *et al.* 2005), has been extensively studied for cohesionless granular materials and has served as a benchmark for both discrete (Staron & Hinch 2005; Lacaze, Phillips & Kerswell 2008; Kermani, Qiu & Li 2015) and continuum simulations (Lagrée, Staron & Popinet 2011). When the grains are released, the granular mass spreads and stops at a finite distance (Lajeunesse *et al.* 2005). It has been shown that the morphology of the deposit is mainly controlled by the initial aspect ratio of the column, and scaling laws have been obtained for the run-out distance and the final height, which are independent of the material properties.

The problem of the collapse of a column has also been investigated in the case of a pure viscoplastic material. The different failure modes and the existence of non-deformed regions during the flow have been reported, in order to better understand how the run-out depends on the aspect ratio and yield stress (Chamberlain *et al.* 2001; Liu *et al.* 2016).

The case of cohesive materials lies between these two extreme cases, as they exhibit both a yield stress like viscoplastic materials and friction like granular materials. Several studies have investigated the influence of cohesion on the dynamics of granular collapse. Experimentally, Mériaux & Triantafillou (2008) have studied the collapse of fine powders and showed that cohesion does not modify the scaling laws of the run-out but modifies the prefactors. Artoni *et al.* (2013), and more recently Li *et al.* (2021), have studied the collapse of wet granular media and how the dynamics depends on both the particle diameters via the Bond number and the water content. Using the discrete element method and an irreversible adhesive force model between particles to mimic solid bridges, Langlois *et al.* (2015) have shown how fragmentation occurs during the collapse and how it decreases the run-out distance. Abramian *et al.* have analysed the stability criterion (Abramian, Staron & Lagrée 2020) and the roughness of the free surface (Abramian, Lagrée & Staron 2021) of the final deposit, which increases when increasing the adhesive forces between the grains.

In this paper, we revisit the problem of the collapse of a cohesive granular medium by performing experiments using the new CCGM, and by confronting the measurements to predictions from continuum simulations using a simple rheological description obtained by adding a constant cohesive stress to the $\mu(I)$ rheology. Although the rheology of cohesive materials is known to be more complex (Badetti *et al.* 2018; Macaulay & Rognon 2021; Mandal, Nicolas & Pouliquen 2021), this approach is a first attempt to capture cohesive effects in a continuum model. After the description of the experimental procedure

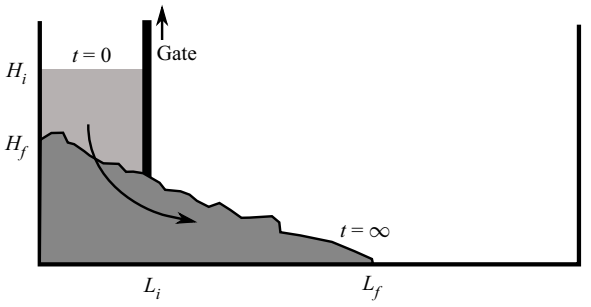

Figure 1. Sketch of the experimental set-up showing the initial granular column of length L_i and height H_i (light grey) and the final deposit of length L_f and height H_f (dark grey).

and the numerical methods in § 2, we focus on the stability condition in § 3, and on the failure mode of the pile in § 4, where we confront the observation to the prediction of a Mohr–Coulomb model. The role of cohesion on the dynamics of the flow, on the typical velocities and on the shape of the final deposit are discussed in § 5, before concluding in § 6.

2. Experimental and numerical methods

2.1. *Experimental set-up and methods*

In our experiments, the CCGM is made of glass beads of diameter $d = 800 \pm 60$ µm coated with a PBS polymer. To tune the cohesion, we vary the average thickness b of the coating in the range $0 < b < 400$ nm. From equation (7) in Gans *et al.* (2020), this corresponds to a static cohesive stress τ_c in the range $0\ \text{Pa} < \tau_c < 65\ \text{Pa}$. In the following, the cohesion is characterized through the cohesion length ℓ_c defined as

$$\ell_c = \frac{\tau_c}{\phi \rho g}, \tag{2.1}$$

which corresponds to the characteristic length for which the hydrostatic pressure $P = \phi \rho g \ell_c$ is equal to the cohesive stress τ_c. In this paper, the particle density is $\rho = 2600\ \text{kg m}^{-3}$, the volume fraction is $\phi \approx 0.58$ and g is the acceleration due to gravity. As a result, the range of cohesive lengths investigated in this study is $0 \leqslant \ell_c \leqslant 4.1$ mm.

A sketch of the experimental set-up is shown in figure 1. It consists of a rectangular channel of length 62 cm, width 15.4 cm and height 31 cm. A mass M of cohesive grains is retained on the left side of the box by a removable gate, which can slide upwards. The rectangular channel is built with poly(methyl methacrylate) (PMMA) plates, and the bottom plate is made rough by gluing particles of the same size as the flowing particles. Since the PBS-coated particles have a very low friction coefficient with PMMA, there is no significant lift nor tangential stress observed either when opening the gate, or on the sidewalls. Different initial columns are used with a length L_i in the range $2.54\ \text{cm} < L_i < 12.7\ \text{cm}$ and a height H_i in the range $1\ \text{cm} < H_i < 23\ \text{cm}$. As a result, the aspect ratio $a = H_i/L_i$ varies in the range $0.7 < a < 6.6$. At time $t = 0$, the gate is rapidly removed vertically, and the granular mass spreads until it reaches a new static configuration at long time. The final deposit is characterized by its length L_f and its height H_f. The granular collapse is recorded with a high-speed camera (Phantom VEO 710) at 300 frames per second. A vertical laser sheet illuminates the vertical central plane of the channel, providing a measurement of the pile profile during the flow. Using image

processing software, the spatio-temporal evolution of the profile is computed, and the front velocity V and the final deposit geometry are measured.

2.2. *Numerical methods*

In parallel with the experiments, we performed numerical simulations based on the two-dimensional Navier–Stokes solver Basilisk, an open-source library (www.basilisk.fr) using an adaptive mesh and a volume-of-fluid method. The granular material is considered as an incompressible fluid, with a non-Newtonian frictional rheology. Without cohesion, it has been shown that the collapse is captured by the simple $\mu(I)$ constitutive law (Lagrée *et al.* 2011). The stress tensor is given by $\sigma_{ij} = -P\delta_{ij} + \tau_{ij}$, where P is the pressure and τ_{ij} is the deviatoric stress given by

$$\tau_{ij} = \mu(I)P\frac{\dot{\gamma}_{ij}}{|\dot{\gamma}|}. \tag{2.2}$$

Here $\dot{\gamma}_{ij}$ is the shear-rate tensor, $|\dot{\gamma}| = \sqrt{\dot{\gamma}_{ij}\dot{\gamma}_{ij}/2}$ is its second invariant and the friction coefficient μ is a function of the dimensionless inertial number I,

$$\mu(I) = \mu_s + \frac{\Delta\mu}{I_0/I + 1}, \quad \text{with} \quad I = \frac{|\dot{\gamma}|d}{\sqrt{P/\rho}}, \tag{2.3}$$

where $\mu_s = 0.4$ is extracted from Gans *et al.* (2020) and observed to be independent of b, $\Delta\mu = 0.12$ and $I_0 = 0.3$.

In this study, where cohesion plays an important role, we extend this rheological model by adding a constant cohesive stress τ_c so that the deviatoric stress τ_{ij} becomes (see Abramian *et al.* (2020) for numerical details)

$$\tau_{ij} = [\tau_c + \mu(I)P]\frac{\dot{\gamma}_{ij}}{|\dot{\gamma}|}. \tag{2.4}$$

This expression assumes that adhesion does not modify the shear-rate-dependent frictional part of the constitutive law, which is a strong simplification. However, during collapse, the rate-dependent part of the rheology appears to play a negligible role (see the Appendix), which motivates our choice of this simple constitutive law.

In the following, when comparing the simulations to the experiments, the value of τ_c in the numerical code is equal to its experimental value. The parameters of the friction law $\mu(I)$, when not specified, are chosen from a calibration based on the cohesionless case: $\mu_s = 0.4$, $\Delta\mu = 0.12$ and $I_0 = 0.3$. The influence of these numerical parameters is discussed in the Appendix. It should be emphasized that, in the numerical method, the plastic criterion and the existence of a yield stress are not strictly captured. A regularization method is used where a cutoff of the viscosity to a finite but high value is introduced for low values of shear rate (Abramian *et al.* 2020).

2.3. *Control parameters*

The dynamics of the cohesive granular collapse is *a priori* controlled by three dimensionless numbers: the aspect ratio of the initial column $a = H_i/L_i$, the relative magnitude of the cohesion stress compared to the gravity stress given by the ratio of the cohesive length to the height of the columns ℓ_c/H_i, and the number of particles in the column H_i/d. Considering the continuum model (2.4), it is easy to show that the latter parameter plays a role only in the inertial number where the particle diameter explicitly

appears, i.e. in the dependence of the rheology on the shear rate. Thus, in the limit of quasi-static regimes with negligible inertial number as studied in this paper, H_i/d is expected to play a limited role. In this regime, the system is therefore mainly controlled by only two parameters, $a = H_i/L_i$ and ℓ_c/H_i, which are chosen to be equal in the simulation and in the experiments when confronting the experimental observation to the numerical prediction.

2.4. *Qualitative observations*

When the gate of the experimental set-up is removed, three different behaviours are observed, depending on the aspect ratio of the column and on the cohesion of the material. When the column is not high enough, it remains static, showing that a minimum height of cohesive material is required to trigger the flow (figure 2*a*). For a slightly higher column, the material breaks along a well-defined failure plane having its origin at the foot of the pile, leading to the collapse of the top right corner of the column (figure 2*b*), the rest of the pile remaining undeformed. For a sufficiently high column and/or for a sufficiently weak cohesive force between particles, the collapse starts at the right corner but extends to the bulk, leading to the spreading of the granular mass until a new static configuration is reached (figure 2*c*). The final deposit surface reveals a roughness reminiscent of undeformed clusters during the flows (Langlois *et al.* 2015), which increases when increasing the cohesion (Abramian *et al.* 2020). In particular, the upper right corner of the initial column seems to be carried by the flow without being sheared or deformed and is present in the final deposit (figure 2*c*). The same phenomenology is observed in simulations, as shown in figure 2.

However, the origin of the free-surface roughness in the continuous simulations remains unclear and would require a specific study. We observed that the irregularities depend on the mesh size, suggesting that their development might be related to the ill-posed behaviour of the $\mu(I)$ rheology (Barker *et al.* 2015). However, we verified that the dynamics studied in the sequel are independent of mesh size, and calculations were performed with a typical mesh size of 5.86×10^{-3} (52 μm) in the column.

3. Column stability

To interpret the initiation of the flow and the failures observed in both experiments and simulations, we express the stability condition of a granular column in the framework of a simple cohesive Mohr–Coulomb model.

3.1. *Theoretical failure conditions*

The failure of hills has been the subject of many studies in the soil mechanics literature (Fredlund & Krahn 1977; Halsey & Levine 1998; Chen, Yin & Lee 2003; Duncan, Wright & Brandon 2014). Here, we restrict our analysis to the simple assumption that failure occurs along a straight plane, following the work of Restagno, Bocquet & Charlaix (2004). The three different configurations depicted in figure 3 are analysed: an infinitely wide rectangular pile, a truncated wide pile and a rectangular pile of finite width.

3.1.1. *Rectangular pile with a small aspect ratio*

We first consider a cohesive rectangular column of height H_i and width $L_i \gg H_i$. A corner delimited by the slip plane having its origin at the bottom right base and inclined at an

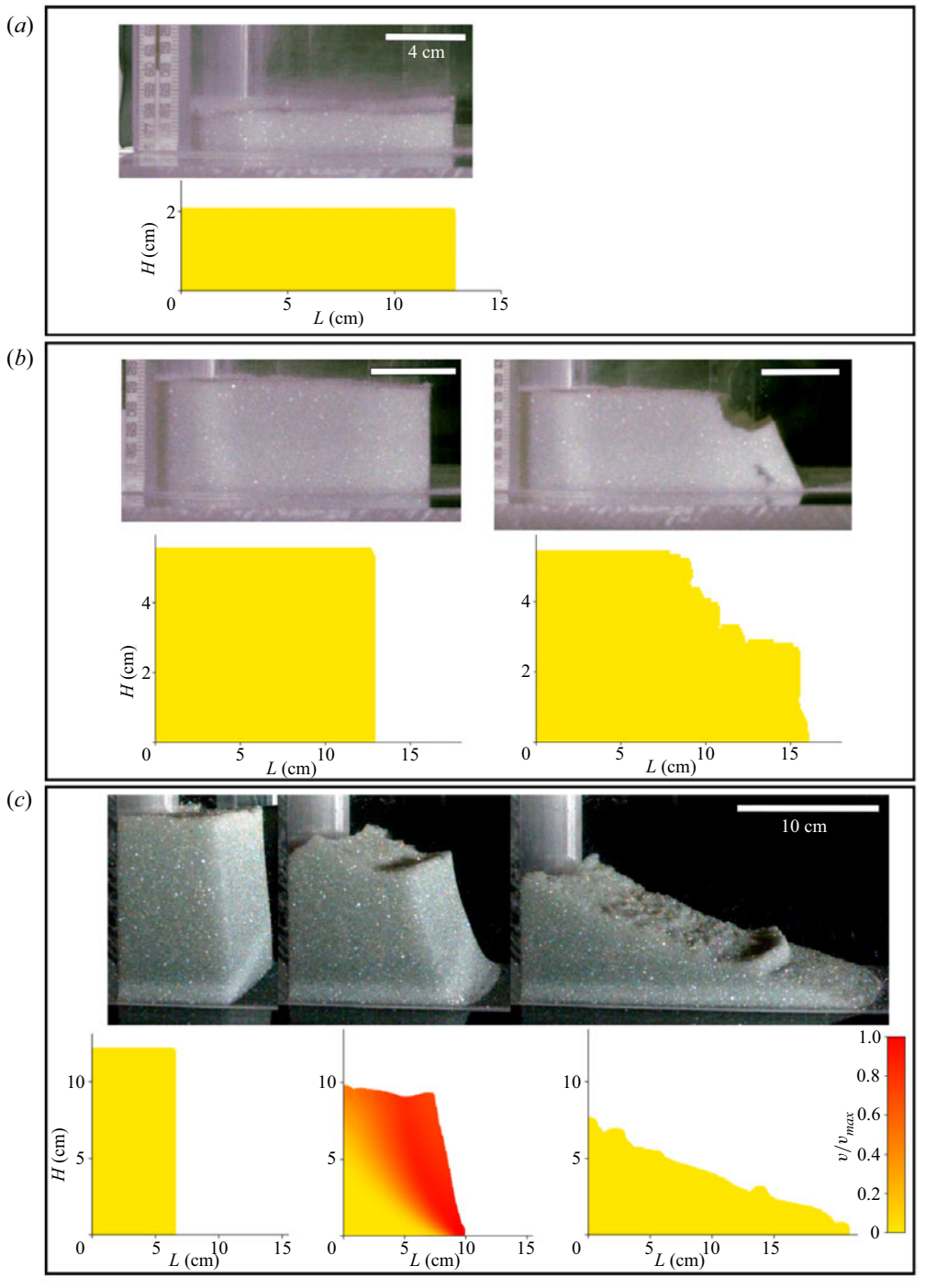

Figure 2. Experimental observations (top grey pictures) and numerical simulation (bottom colour pictures) of the collapse of a cohesive granular column. (*a*) A stable column with small aspect ratio ($a = 0.08$, $\ell_c = 4.1$ mm, $\ell_c/H_i = 0.2$). (*b*) Partial collapse for a moderate aspect ratio ($a = 0.43$, $\ell_c = 4.1$ mm, $\ell_c/H_i = 0.08$) with a well-defined slip plane. (*c*) Collapse of the column ($a = 1.9$, $\ell_c = 2.8$ mm, $\ell_c/H_i = 0.025$), where we observe a 'surfing wedge' coming from the top right corner being transported during the flow. The white scale bar corresponds to 4 cm in panels (*a*) and (*b*), and to 10 cm in panel (*c*).

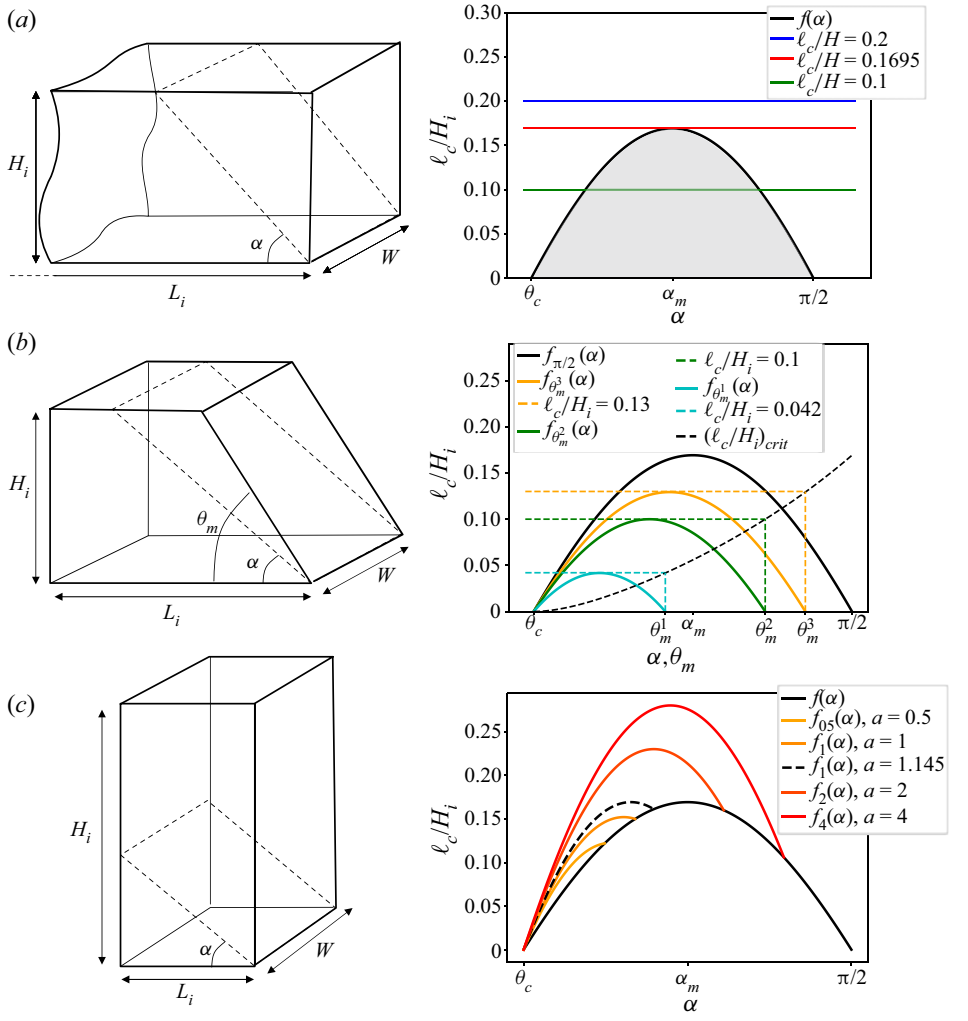

Figure 3. Theoretical analysis of the stability of columns using a cohesive Mohr–Coulomb criterion. (*a*) Wide column: the corner delimited by the plane inclined at an angle α is stable when the cohesion level ℓ_c/H_i is above the black curve $f_{\theta_c}(\alpha)$ in (3.3). The blue line corresponds to a cohesion level leading to stable column, the red line to a marginally stable column where a single angle $\alpha_m = \theta_c/2 + \pi/4$ is unstable, and the green line to an unstable column. The grey area corresponds to the unstable angles. (*b*) Truncated pile: the different curves correspond to the stability function $f_{\theta_c,\theta_m}(\alpha)$ in (3.5) for different values of the free-surface inclination θ_m (i.e. $\theta_m^1 = 50°$, $\theta_m^2 = 71.4°$, $\theta_m^3 = 80°$). The dashed line is the function $(\ell_c/H_i)_{crit}(\theta_m)$ in (3.6) above which the truncated pile is stable. (*c*) Tall column: the stability curves for various aspect ratios a given by $f_{\theta_c,a}(\alpha)$ in (3.8) for $\alpha < \arctan a$ and by $f_{\theta_c}(\alpha)$ in (3.3) for $\alpha > \arctan a$.

angle α from the horizontal (figure 3*a*) is stable according to a cohesive Mohr–Coulomb criterion if the following condition is satisfied:

$$Mg \sin\alpha \leq S\tau_c + \mu_s Mg \cos\alpha, \tag{3.1}$$

where M is the mass of material above the slip plane, S is the area of the failure surface, μ_s is the static friction angle and τ_c is the cohesive stress. In the configuration of figure 3(*a*), we can write $M = \rho W {H_i}^2/(2\tan\alpha)$ and $S = WH_i/\sin\alpha$, where W is the thickness of the

pile. The pile is then stable when

$$\frac{\rho g H_i}{2\tan\alpha}\sin\alpha\,(\sin\alpha-\mu_s\cos\alpha)\le\tau_c, \tag{3.2}$$

which can be expressed using the cohesive length ℓ_c and the friction angle $\theta_c=\arctan(\mu_s)$,

$$f_{\theta_c}(\alpha)=\frac{\cos\alpha\sin(\alpha-\theta_c)}{2\cos\theta_c}\le\frac{\ell_c}{H_i}. \tag{3.3}$$

The function $f_{\theta_c}(\alpha)$ is shown in figure 3(*a*) for $\mu_s=0.4$ corresponding to $\theta_c=21.8°$. This function is a symmetric curve centred at $\alpha_m=\theta_c/2+\pi/4$, where it reaches its maximum value $f_{\theta_c}(\alpha_m)\approx 0.17$, and becomes zero for $\alpha=\theta_c$ and $\alpha=\pi/2$. In this plot, a point $(\alpha,\ell_c/H_i)$ below the curve corresponds to an unstable corner. A high cohesion level $\ell_c/H_i>0.17$ corresponds to a stable pile (blue line) for which the stability criterion (3.3) is fulfilled whatever the slip angle α. The value $\ell_c/H_i=0.17$ corresponds to the marginally stable pile, which will break along the slip plane inclined at α_m (red line). A low cohesion level $\ell_c/H_i<0.17$ (green line) corresponds to an unstable column that may fail at any angle for which $f_{\theta_c}(\alpha)>\ell_c/H_i$ (grey zone in figure 3*a*).

3.1.2. *Truncated pile*

The previous analysis can be generalized to the case of a truncated pile, with a missing corner inclined at an angle θ_m (figure 3*b*). Studying this geometry is interesting, as it may provide information about the stable final deposit shape. By evaluating the mass of material M located between the slip plane inclined at an angle α and the free surface inclined at an angle θ_m, one can derive the following expression for the stability criterion:

$$\frac{1}{2}\rho g H_i\left(\frac{1}{\tan\alpha}-\frac{1}{\tan\theta_m}\right)\sin\alpha\,(\sin\alpha-\mu\cos\alpha)\le\tau_c. \tag{3.4}$$

Again using ℓ_c and θ_c, this equation may be rewritten as

$$f_{\theta_c,\theta_m}(\alpha)=\frac{\sin(\theta_m-\alpha)\sin(\alpha-\theta_c)}{2\cos\theta_c\sin\theta_m}\le\frac{\ell_c}{H_i}. \tag{3.5}$$

The different stability limits in the plane α versus ℓ_c/H_i for different truncated angles θ_m are plotted in figure 3(*b*). The graphs of the function $f_{\theta_c,\theta_m}(\alpha)$ are curves centred at $(\theta_c+\theta_m)/2$ and vanishing at $\alpha=\theta_c$ and $\alpha=\theta_m$. The rectangular pile is recovered for $\theta_m=\pi/2$. The maximum of the $f_{\theta_c,\theta_m}(\alpha)$ gives the value of the critical cohesion level $(\ell_c/H_i)_{crit}(\theta_m)$ below which the pile truncated at angle θ_m is unstable, given by the following equation:

$$\left(\frac{\ell_c}{H_i}\right)_{crit}(\theta_m)=\frac{1-\cos(\theta_m-\theta_c)}{4\cos\theta_c\sin\theta_m}. \tag{3.6}$$

This function $(\ell_c/H_i)_{crit}(\theta_m)$ is plotted in figure 3(*b*) as the black dashed line. A pile truncated at an angle θ_m and for a cohesion level ℓ_c/H_i such that the point $(\theta_m,\ell_c/H_i)$ is below this line, is unstable.

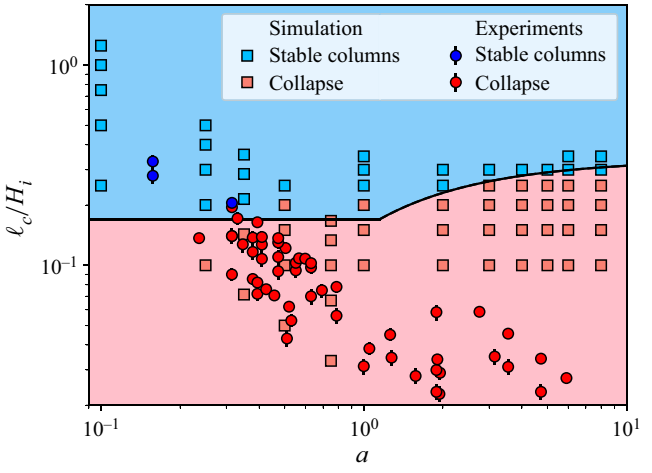

Figure 4. Stability diagram in the aspect ratio a versus cohesion level ℓ_c/H_i plane for a cohesive granular column. The black curve is the limit of stability. Circles corresponds to experiments, squares to simulation and blue (red) symbols correspond to stable (unstable) columns.

3.1.3. *Rectangular pile with a large aspect ratio*

The last case of interest is the case when the aspect ratio of the pile is large and such that the slip plane no longer intersects the top free surface but the left side of the pile, i.e. when $\arctan a \geq \alpha$ (figure 3*c*). In this case, $M = \rho W L_i (H_i - \frac{1}{2} L_i \tan\alpha)$ and $S = W L_i / \cos\alpha$, and the stability criterion of the column is given by

$$\rho g \left(H_i - \frac{L_i \tan\alpha}{2} \right) \cos\alpha \, (\sin\alpha - \mu_s \cos\alpha) \leq \tau_c, \tag{3.7}$$

which can be written as

$$f_{\theta_c,a}(\alpha) = \left(1 - \frac{1}{a} \frac{\tan\alpha}{2} \right) \cos^2\alpha \, (\tan\alpha - \tan\theta_c) \leq \frac{\ell_c}{H_i}. \tag{3.8}$$

The stability criterion in this case depends on the aspect ratio a and is given by the function $f_{\theta_c,a}(\alpha)$, which is plotted as curves starting at $(\alpha = \theta_c, 0)$ and presenting a maximum. This maximum increases when increasing the aspect ratio. When the slip angle α reaches the $\arctan a$ value, i.e. the slip plane no longer reach the left vertical side of the column, the stability criterion is no longer given by the $f_{\theta_c,a}(\alpha)$ function but by the low-aspect-ratio function $f_{\theta_c}(\alpha)$ in (3.3). For a given aspect ratio a, the stability of the column is thus given by a curve made of two parts, as shown in figure 3(*c*), its absolute maximum giving the critical cohesion level below which the pile is unstable. At low aspect ratio, the first part of the curve (colour curves in figure 3*c*) is lower than the second part (black curve), and the stability is controlled by a constant cohesion level, independent of a. When a becomes greater than 1.145 (black dashed line in figure 3*c*), the maximum is given by the first maximum corresponding to a mode of failure crossing the pile from one side to another. A stability limit can then be plotted in the $(a, \ell_c/H_i)$ plane, as shown by the black curve in figure 4, separating the stable region (blue) from the region where collapse occurs (pink). The discontinuity between the two geometrical possibilities of failure occurs at $a \approx 1.145$.

In conclusion, three stability criteria have been derived, depending on the aspect ratio of the rectangular column, or if the pile is truncated with an angle θ_m. In the next section, we test the stability criteria using experimental observations and numerical simulations.

3.2. *Experimental and numerical observations*

We first investigated experimentally the condition for a collapse of the pile after the opening of the gate. Numerous experiments were done, varying both the aspect ratio a and the cohesive strength ℓ_c/H_i. The results are plotted in figure 4 as circles, with the following colour code: red indicates that a collapse occurs, and blue indicates that the column remains stable. Experimentally, we were not able to investigate the high-aspect-ratio and large ℓ_c/H_i limit, as, for the range of ℓ_c accessible with our beads, it would correspond to narrow piles with only few particles in the width.

We can further explore this diagram using numerical simulations. Stable and unstable columns are discriminated by using two criteria: the column is stable either if its final run-out does not exceed 1 % of the initial length, or if the maximum viscosity is reached everywhere in the early stage of the collapse. Overall, these two criteria lead to the same results. The numerical results are data taken from Abramian *et al.* (2020) and data from new computations. The results are plotted figure 4 as squares, with the same colour code as for the circles.

Finally, both experimental and numerical results show a good agreement with the Mohr–Coulomb stability criterion, showing that the limit of stability of a cohesive granular pile is well captured by a simple Mohr–Coulomb model.

4. Collapse angles

The above theoretical stability analysis predicts whether a column of aspect ratio a and cohesion level ℓ_c/H_i between grains is stable or unstable (solid line in figure 4). It also provides an estimate of the failure angles α or a range of possible failure angles, which is the scope of the present section.

If the failure angle $\alpha_m = \theta_c/2 + \pi/4$ is well predicted at the stability threshold (when $\ell_c/H_i = (\ell_c/H_i)_{crit}(\pi/2)$), the theoretical analysis does not predict the angle for lower cohesion or larger column, i.e. when the collapse occurs far from the stability threshold. Instead, the analysis predicts a whole range of unstable angles (grey area, figure 3*a*). To investigate this range and understand how the column breaks, in this section we focus on two characteristic angles: we identify the initial angle of failure α_i at the onset of collapse, and a final angle α_f at the end of collapse, defined as the angle of the plane below which no grain has moved during the entire collapse time (see the inset in figure 5).

These two different angles have been measured in both the experiments and numerical simulations. Experimentally, to determine α_i, we compare a reference image of the static column with the subsequent images at the onset of the flow using an image subtraction process enhanced with a threshold filter. Numerically, we threshold the velocity field at the initiation of the flow. The angle α_f is experimentally measured through an image difference process between the initial reference image and the images recorded at the end of the collapse, and numerically by thresholding the integral of the velocity field during the whole dynamics. The experimental and numerical results are reported in figure 5, where we restrict the analysis to the small-aspect-ratio configuration (figure 3*a*).

The initial failure angle α_i measured in the simulations (open red circles) is constant whatever the parameters, and is always close to the critical angle $\alpha_m = \theta_c/2 + \pi/4 \approx 55^\circ$

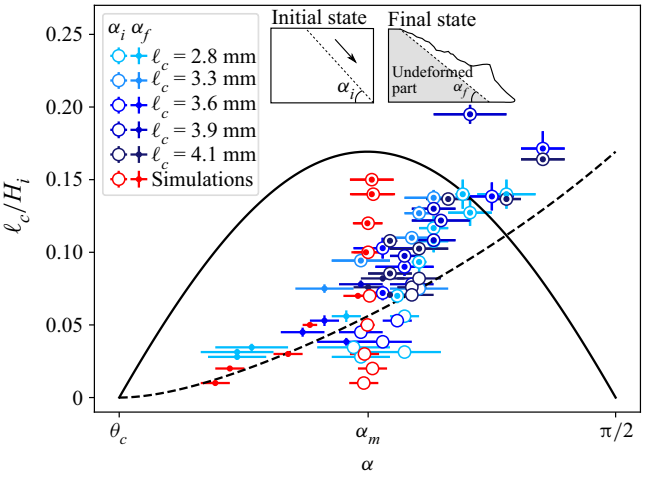

Figure 5. Measurements of the initial failure angle α_i (open circles) and final angle of stability α_f (filled dots) for different cohesion levels ℓ_c/H_i. Red symbols are from numerical simulations, and blue symbols are from experiments. The continuous line is given by (3.3). The dashed line corresponds to (3.6), giving the limit of stability of truncated piles.

predicted by the Mohr–Coulomb theory for the incipient failure mode. For low cohesion, the final failure angle α_f (red dots), delimiting the region where grains never move during the collapse, is lower than α_i, because the grains are entrained by the flow. This corresponds to a friction-dominated regime. For higher cohesion, the final failure angle approaches α_i until the two are equal: this is a cohesion-dominated regime. Here, only the first unstable corner flows while the rest of the pile remains static, as illustrated in figure 2(*b*). The transition between the two regimes occurs for $\ell_c/H_i \sim 0.08$.

The observation is slightly different in experiments. Although we identify the two regimes, the initial failure angle (blue open circles) is not constant whatever the cohesion level. It is close to the critical angle α_m at low cohesion, but the experimental α_i increases when increasing the cohesion and becomes larger than what is predicted in the simulation. Interestingly, in experiments, α_f is close to the critical curve computed theoretically for the stability of truncated piles ((3.6), dashed line in figure 5), meaning that the final shape of the column is close to the marginally stable shape. We assume that α_f compares with θ_m of (3.6) since it represents the lower bound of stability despite the flow above it. The discrepancy between simulations and experiments for high cohesion levels may have different origins. A first origin could be that, in the experiment, the gate is not instantaneously removed. The time needed to open the door might induce a stress relaxation at the early stage of the collapse, which is not present in the numerical simulations, where the stresses are instantaneously released. Another source of discrepancy could be that the constitutive law chosen in the simulation is too simple, and other effects, such as normal stress differences, transient effects and/or dilatancy effects, are missing.

5. Collapse dynamics, run-out length and final deposit

5.1. *Velocity of the front*

Once the gate is removed, the column collapses and a granular front propagates. The profile of the pile during the collapse can be extracted in experiments from the high-speed

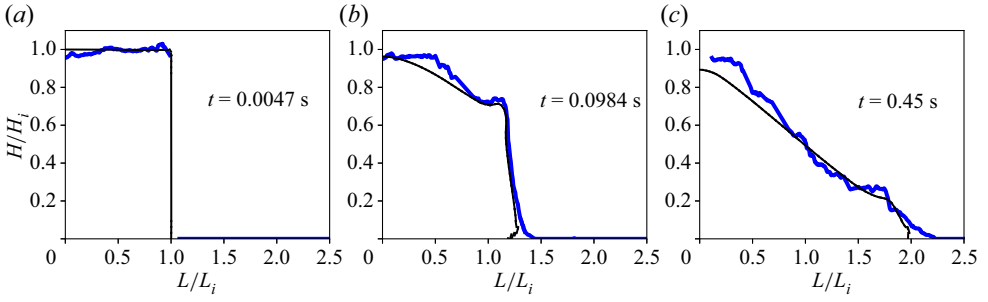

Figure 6. Comparison between the numerical (black) and experimental (blue) profiles of the granular pile at different times for $H_i = 8.9$ cm, $a = 1$ and $\ell_c = 2.8$ mm.

movie and the laser sheet projection. A typical run is presented in figure 6 showing both the experimental and numerical results for the same parameters for a weakly cohesive material (aspect ratio $a = 1$, $\ell_c/H_i = 0.0314$). Using the same parameters in simulation (cf. § 2.2), we find a fairly good agreement between the experiments and the numerical predictions for the dynamics of the pile profile during the collapse. The dynamics of the front and its position $L(t)$ can be determined by measuring the location $L(t)$ of the foot of the pile in both experiments and simulations. The experimental results $L(t) - L_i$ are plotted as solid lines in figure 7(*a*), for $\ell_c = 0$ (cohesionless material), $\ell_c = 2.8$ mm and $\ell_c = 3.6$ mm, for an aspect ratio $a = 1$. As a comparison, numerical simulations with the same cohesion levels and the same aspect ratio are plotted with dashed lines. We observe that, after a short acceleration step, the front travels at a constant velocity before decelerating and eventually reaching a static position. The comparison between the experimental and numerical results shows a good agreement from the beginning to the end of the steady state. The agreement is very good for the cohesionless granular experiment (light blue curves), showing that the granular collapse is well described by the continuous numerical code with the $\mu(I)$ rheology. However, in the case of cohesive materials, a difference is observed between experiments and simulation when the flow slows down and stops. The final run-out length is systematically shorter in the numerical simulations for cohesive materials compared to the experiments, as can also be observed in figure 6.

Another discrepancy is observed at lower aspect ratio ($a = 0.5$), close to the stability limit (inset of figure 7(*a*) for a smaller aspect ratio and $\ell_c = 3.6$ mm), for which the experiments reveal a delay between the opening of the gate and the initiation of the flow. This delay is not observed in the simulation, and may be reminiscent of more complex rheological features induced by the thick polymer coating, leading to some creeping phenomena not taken into account in the simple rheological model used in the simulation.

Despite this discrepancy, the velocity V_{max} of the front is quantitatively predicted by the simulation, as shown in figure 7(*b*). The velocity V_{max} is defined as the velocity at the inflection point in the $L(t) - L_i$ curves of figure 7(*a*). The velocity increases with the aspect ratio up to a plateau when $a \approx 3$. The graph also shows that the velocity decreases when the cohesion increases.

5.2. *Run-out and final deposit*

Once the kinetic energy of the collapse is fully dissipated, we measure the final deposit and focus on the final run-out length, $L_f = L_i + \Delta L$. As shown by Lajeunesse *et al.* (2005), the run-out length and the final height of a cohesionless granular material scale as power laws

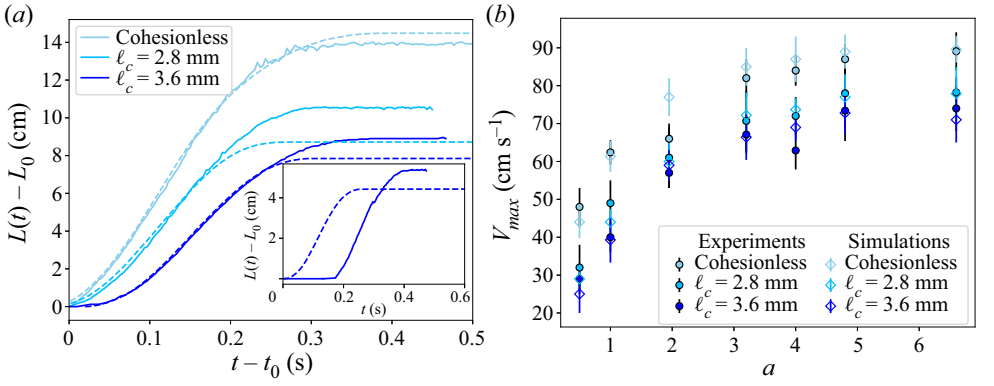

Figure 7. (*a*) Time evolution of the front position for different cohesion levels in experiments (continuous curves) and simulations (dashed curves) for an aspect ratio $a = 1$. Inset: results for $a = 0.5$ showing the existence of a significant delay in the experiments before the collapse occurs for the most cohesive material (dark blue, $\ell_c = 3.6$ mm). (*b*) Velocity of the front V as a function of the aspect ratio a for different cohesion levels. The colour code is the same as in panel (*a*).

of the aspect ratio a:

$$\frac{\Delta L}{L_i} \propto \begin{cases} a & \text{for } a \leq 3, \\ a^{2/3} & \text{for } a \geq 3, \end{cases} \quad \text{and} \quad \frac{H_f}{L_i} \propto \begin{cases} a & \text{for } a \leq 0.7, \\ a^{1/3} & \text{for } a \geq 0.7. \end{cases} \tag{5.1a,b}$$

The results for L_f and H_f obtained with cohesionless and cohesive materials are plotted in figures 8(*a*) and 8(*b*), respectively, where filled symbols are experimental results and open symbols are numerical results. The run-out length L_f decreases when increasing the cohesion, but the final height H_f remains constant. However, the power laws (5.1*a*,*b*) seem unchanged compared to the cohesionless case, as seen by the a^1 and $a^{2/3}$ slopes on the graph, although the range of aspect ratio investigated is too narrow to conclude firmly on the scalings. These results are in agreement with previous observations for powders (Mériaux & Triantafillou 2008), showing that cohesion only changes the prefactor on the run-out length (5.1*a*,*b*), without changing the exponent on the aspect ratio. Unfortunately, understanding this prefactor analytically is not trivial, and is out of the scope of the present paper.

As discussed previously, the simulations for the cohesive material systematically underestimate the final run-out compared to the experiments. Looking more precisely at the morphology of the free surface at the end of the flow reveals that the discrepancy is localized at the tip of the deposit. The no-slip boundary condition applied in the simulation at the contact line may be a source of additional dissipation explaining the difference between simulation and experiments. We show in the Appendix that, by adjusting the parameters of the rheological model, μ_s, $\Delta\mu$ and I_0, the run-out can be adjusted, but we found no set of parameters able to predict both cohesionless and cohesive systems.

6. Discussion and conclusion

In this paper, we studied the dynamics of the collapse of a column of cohesive granular material both experimentally, using a CCGM made of polymer-coated particles, and numerically, using a continuous approach based on a cohesive viscoplastic rheology.

The first effect of cohesion is the stabilization of the granular column with a stability criterion that depends on the aspect ratio and the cohesion level. A stability criterion and

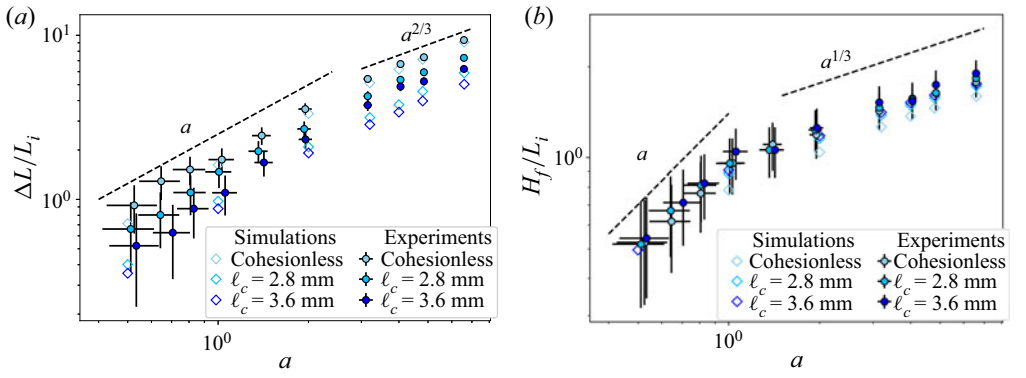

Figure 8. (*a*) Normalized run-out length $\Delta L/L_i$ as a function of the aspect ratio a for different cohesion levels for both experiments and simulations. (*b*) Normalized height of final deposit H_f/H_i as a function of the aspect ratio a.

an angle of failure have been measured and compared with a simple theoretical approach based on a Mohr–Coulomb stability criterion assuming a planar slip line. It would be interesting in future work to go beyond this approximation, and analyse more precisely the mode of failure of the column, in the spirit of studies done to understand the collapse of a column of Bingham material (Chamberlain *et al.* 2001; Liu *et al.* 2016). How the presence of both a plastic yield stress and a frictional stress changes the slip lines is an open question.

A second effect of cohesion is the increase of the dissipation during the flow, leading to a slower spreading of the material and a shorter run-out length. A striking effect of the cohesion on the collapse of the granular column is the presence of a 'surfing wedge' on the top corner of the column. It acts as a dead volume transported passively by the granular flow underneath.

The comparison of the results (stability of the column, run-out length, collapse velocity) between the experiments and the continuous numerical simulation reveals a relatively good agreement, despite some discrepancies. This shows that the main features of the cohesive granular collapse are captured by simply adding a constant cohesive yield stress to the cohesionless granular rheological model. Differences between experiments and simulations were observed for large cohesion levels, for which the initial failure angle is higher in experiments than in simulation, the run-out is underestimated in the simulation, and a delay before collapse is observed in experiments and not captured in simulations. These differences may come from an oversimplified description of the rheological properties of the cohesive granular material. Additional studies with other configurations more sensitive to rheological details than column collapse would be interesting to further investigate the rheological properties of the material.

Funding. This research was supported by Agence Nationale de la Recherche through the grant NR-17-CE08-0017 under the COPRINT (Cohesive Powders Rheology: Innovative Tools) project.

Declaration of interests. The authors report no conflict of interest.

Author ORCIDs.
A. Gans https://orcid.org/0000-0001-5131-7145;
A. Abramian https://orcid.org/0000-0002-0937-2797;
P.-Y. Lagrée https://orcid.org/0000-0002-3931-6622;
A. Sauret https://orcid.org/0000-0001-7874-5983;

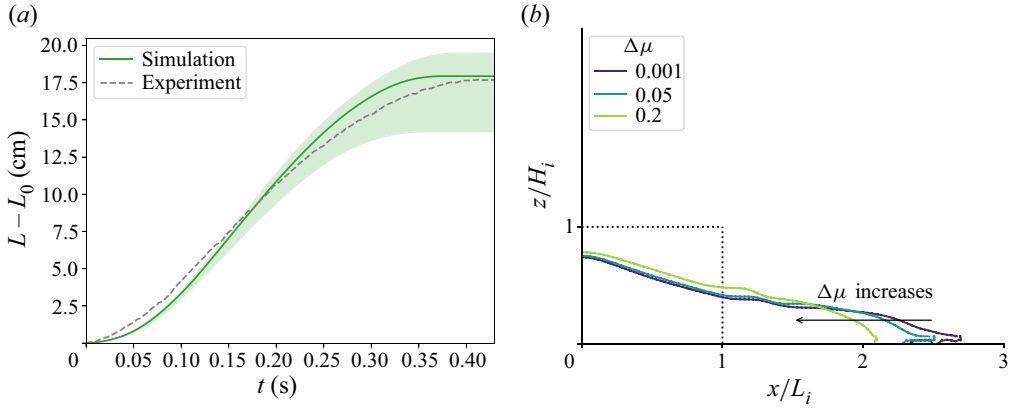

Figure 9. (*a*) Experimental and numerical front position $L(t)$ of the collapse for $\ell_c = 2.8$ mm, $I_0 = 0.1$ and $a = 1$. The green area is obtained by varying the parameter $\Delta\mu$ from 0 to 0.2, and the green line is the best agreement for the velocity and the run-out. (*b*) Final profiles for three values of $\Delta\mu$.

O. Pouliquen https://orcid.org/0000-0002-2246-1137;
M. Nicolas https://orcid.org/0000-0002-4170-8035.

Author contributions. A.G., M.G. and A.S. performed the experiments; A.G., A.A. and P.-Y.L. performed the numerical simulations; all authors contributed equally to analysing data and reaching conclusions, and in writing the paper.

Appendix. Effect of the rheological parameters

The rheological model implemented in the numerical simulations is set by three arbitrary parameters: the static friction coefficient μ_s, the friction coefficient difference $\Delta\mu$, and the inertial number constant I_0 (see (2.3)). In this model, we assume that cohesion does not change these parameters. However, since the run-out length and the final morphology are not well captured by the model, a deeper investigation is needed. The effect of the difference of the friction coefficients $\Delta\mu$ is presented in figure 9(*a*). The distance of the front $L(t)$ is plotted as a function of time for a column of cohesion $\ell_c = 2.8$ mm and an aspect ratio $a = 1$. The green area is obtained by changing the value of $\Delta\mu$ from 0 to 0.2. Figure 9(*b*) shows the associated final profile for different values of $\Delta\mu$. We observe that an increase of $\Delta\mu$ leads to a decrease of the run-out length. Consequently, changing the value of $\Delta\mu$ allows adjusting the final run-out of the cohesive collapse with only a small change in the velocity of the collapse.

The effect of I_0 is plotted in figure 10(*a*) and the associated run-out profile is plotted in figure 10(*b*) for the configuration described above, and a chosen $\Delta\mu = 0.1$. We see that changing the value of I_0 barely changes the dynamics and the final profile of the run-out. Therefore, if the cohesion has an impact on this parameter, we do not expect a major effect.

The last parameter we investigate is the static friction coefficient μ_s. While this parameter has been measured experimentally in a previous study, using inclined-plane experiments (Gans *et al.* 2020), the measurement method was rather different from this set-up. However, after the initiation of the flow, one may suggest that the PBS coating could act like a lubricant, which could decrease the effective μ_s during the flow. An investigation of the effect of the rheological parameter μ_s is presented in figure 11. The distance of the front is plotted as a function of the time for an experiment of aspect ratio $a = 1$ and two

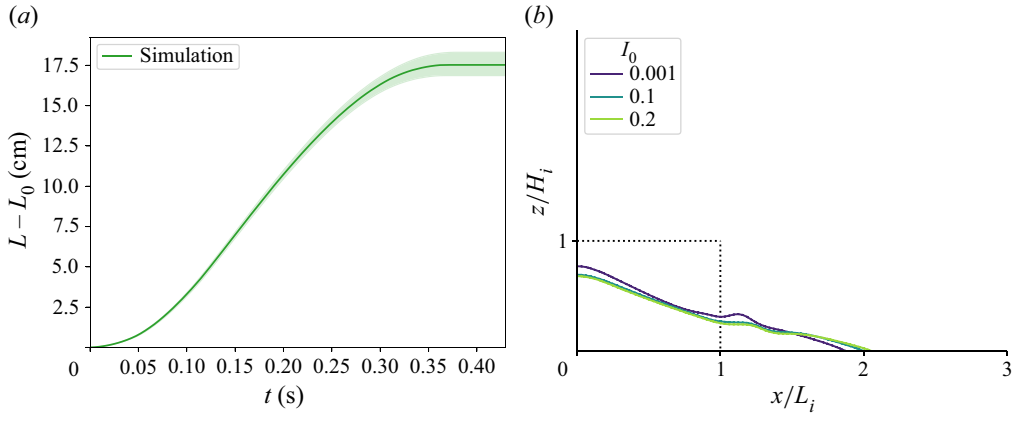

Figure 10. (*a*) Numerical front position $L(t)$ of the collapse for $\ell_c = 2.8$ mm, $\Delta\mu = 0.1$ and $a = 1$. The green area is obtained by varying the parameter I_0 from 0.001 to 0.2, and the green line is the best agreement for the velocity and the run-out. (*b*) Final profiles for three values of I_0.

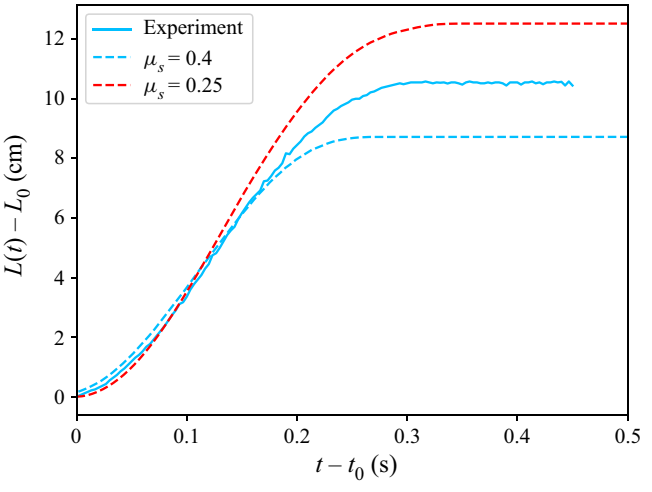

Figure 11. Experimental and numerical front position $L(t)$ of the collapse for $\ell_c = 2.8$ mm, $\Delta\mu = 0.12$, $I_0 = 0.3$ and $a = 1$.

different simulations with $\mu_s = 0.4$ and $\mu_s = 0.25$. We see that a decrease of μ_s leads to an increase of the velocity and of the run-out length.

With this parametric study, we see that a change of $\Delta\mu$ and μ_s may have a significant impact on the dynamics of the collapse, and it may be possible to define an optimal set $(\mu_s, \Delta\mu)$ to fit the experiments. Since, in the experiments, the PBS coating might change the frictional properties during the flow, we do not know if the apparent effect on μ_s and $\Delta\mu$ is due to cohesion or not. These results suggest that a deeper investigation of the rheology of the CCGM is needed to fully understand its dynamical behaviour.

References

Abramian, A., Lagrée, P.-Y. & Staron, L. 2021 How cohesion controls the roughness of a granular deposit. *Soft Matt.* **17** (47), 10723–10729.

ABRAMIAN, A., STARON, L. & LAGRÉE, P.-Y. 2020 The slumping of a cohesive granular column: continuum and discrete modeling. *J. Rheol.* **64**, 1227–1235.

ARTONI, R., SANTOMASO, A.C., GABRIELI, F., TONO, D. & COLA, S. 2013 Collapse of quasi-two-dimensional wet granular columns. *Phys. Rev.* E **87** (3), 032205.

BADETTI, M., FALL, A., HAUTEMAYOU, D., CHEVOIR, F., AIMEDIEU, P., RODTS, S. & ROUX, J.-N. 2018 Rheology and microstructure of unsaturated wet granular materials: experiments and simulations. *J. Rheol.* **62** (5), 1175–1186.

BALMFORTH, N.J. & KERSWELL, R.R. 2005 Granular collapse in two dimensions. *J. Fluid Mech.* **538**, 399–428.

BARKER, T., SCHAEFFER, D.G., BOHÓRQUEZ, P. & GRAY, J.M.N.T. 2015 Well-posed and ill-posed behaviour of the-rheology for granular flow. *J. Fluid Mech.* **779**, 794–818.

BOCQUET, L., CHARLAIX, E., CILIBERTO, S. & CRASSOUS, J. 1998 Moisture-induced ageing in granular media and the kinetics of capillary condensation. *Nature* **87**, 735–737.

CASTELLANOS, A. 2005 The relationship between attractive interparticle forces and bulk behaviour in dry and uncharged fine powders. *Adv. Phys.* **4**, 263–376.

CHAMBERLAIN, J.A., SADER, J.E., LANDMAN, K.A. & WHITE, L.R. 2001 Incipient plane-strain failure of a rectangular block under gravity. *Intl J. Mech. Sci.* **43** (3), 793–815.

CHEN, J., YIN, J.-H. & LEE, C.F. 2003 Upper bound limit analysis of slope stability using rigid finite elements and nonlinear programming. *Can. Geotech. J.* **40**, 742–752.

DUNCAN, J.M., WRIGHT, S.G. & BRANDON, T.L. 2014 *Soil Strength and Slope Stability*, 2nd edn. Wiley.

FOSTER, K.D., BRONLUND, J.E. & PATERSON, T. 2006 Glass transition related cohesion of amorphous sugar powders. *J. Food Engng* **77** (4), 997–1006.

FREDLUND, D.G. & KRAHN, J. 1977 Comparison of slope stability methods of analysis. *Can. Geotech. J.* **14**, 429–439.

GANS, A., POULIQUEN, O. & NICOLAS, M. 2020 Cohesion-controlled granular material. *Phys. Rev.* E **101**, 032904.

HALSEY, T.C. & LEVINE, A.J. 1998 How sandcastles fall. *Phys. Rev. Lett.* **80** (14), 3141.

KAMIYA, H., KIMURA, A., TSUKADA, M. & NAITO, M. 2002 Analysis of the high-temperature cohesion behavior of ash particles using pure silica powders coated with alkali metals. *Energy Fuels* **16** (2), 457–461.

KERMANI, E., QIU, T. & LI, T. 2015 Simulation of collapse of granular columns using the discrete element method. *Intl J. Geomech.* **15**, 04015004.

KONOPKA, L. & KOSEK, J. 2017 Discrete element modeling of electrostatic charging of polyethylene powder particles. *J. Electrostat.* **87**, 150–157.

LACAZE, L., PHILLIPS, J.C. & KERSWELL, R.R. 2008 Planar collapse of a granular column: experiments and discrete element simulations. *Phys. Fluids* **20**, 063302.

LAGRÉE, P.Y., STARON, L. & POPINET, S. 2011 The granular column collapse as a continuum: validity of a two-dimensional Navier–Stokes model with a $\mu(I)$-rheology. *J. Fluid Mech.* **686**, 378–408.

LAJEUNESSE, E., MONNIER, J.B. & HOMSY, G.M. 2005 Granular slumping on a horizontal surface. *Phys. Fluids* **17**, 103302.

LANGLOIS, V.J., QUIQUEREZ, A. & ALLEMAND, P. 2015 Collapse of a two-dimensional brittle granular column: implications for understanding dynamic rock fragmentation in a landslide. *J. Geophys. Res.* **120**, 1866–1880.

LI, P., WANG, D., WU, Y. & NIU, Z. 2021 Experimental study on the collapse of wet granular column in the pendular state. *Powder Tech.* **393**, 357–367.

LIU, Y., BALMFORTH, N.J., HORMOZI, S. & HEWITT, D.R. 2016 Two-dimensional viscoplastic dambreaks. *J. Non-Newtonian Fluid Mech.* **238**, 65–79.

LUBE, G., HUPPERT, H.E., SPARKS, R.S.J. & FREUNDT, A. 2005 Collapses of two-dimensional granular columns. *Phys. Rev.* E **72**, 041301.

MACAULAY, M. & ROGNON, P. 2021 Viscosity of cohesive granular flows. *Soft Matt.* **17** (1), 165–173.

MANDAL, S., NICOLAS, M. & POULIQUEN, O. 2021 Rheology of cohesive granular media: shear banding, hysteresis, and nonlocal effects. *Phys. Rev.* X **11** (2), 021017.

MÉRIAUX, C. & TRIANTAFILLOU, T. 2008 Scaling the final deposits of dry cohesive granular columns after collapse and quasi-static fall. *Phys. Fluids* **20**, 033301.

MITARAI, N. & NORI, F. 2006 Wet granular materials. *Adv. Phys.* **55**, 1–45.

RESTAGNO, F., BOCQUET, L. & CHARLAIX, E. 2004 Where does a cohesive granular heap break? *Eur. Phys. J.* E **14**, 177–183.

SHARMA, R.S., GONG, M., AZADI, S., GANS, A., GONDRET, P. & SAURET, A. 2022 Erosion of cohesive grains by an impinging turbulent jet. *Phys. Rev. Fluids* **7**, 074303.

STARON, L. & HINCH, E.J. 2005 Study of the collapse of granular columns using two-dimensional discrete-grain simulation. *J. Fluid Mech.* **545**, 1–27.